Nanoscale

PAPER

View Article Online
View Journal

Check for updates

Cite this: DOI: 10.1039/d5nr04491j

Octadecene-free colloidal synthesis of $CsPbI_3$ nanocrystals with improved size, shape and phase control

Ruth Pinheiro Muniz,[a,b] Julius Brunner,[a,b] Anatol Prudnikau,[b] Falk Röder,[b] Shivam Singh,[a,b] Raquel Dantas Campos,[a,b] Axel Lubk,[b] Fabian Paulus[b] and Yana Vaynzof *[a,b]

Cesium lead triiodide ($CsPbI_3$) colloidal nanocrystals (NCs) attract significant attention due to their potential for optoelectronic applications. However, they are prone to degrade to the non-photoactive phase (δ-$CsPbI_3$), posing a considerable challenge for industrial use. While many strategies to improve their stability have been explored, the effect of the solvent used during synthesis on the properties of the NCs has received much less attention. This study examines the replacement of the ubiquitously used solvent 1-octadecene (ODE), known to polymerize under mild to high temperatures (120–320 °C), with the less reactive alternative octadecane (ODA). We show that ODA can affect the crystalline growth, size distribution, and stability of $CsPbI_3$ colloidal NCs. While both ODE and ODA form mixtures of cubic α- and orthorhombic γ-$CsPbI_3$ NCs, each phase's prevalence differs depending on the solvent. The use of ODE led to primarily α-phase particles with large polydispersity. In contrast, ODA resulted in a significantly narrower size distribution and a prevalence of γ-$CsPbI_3$ NCs, which are considered more stable. Consequently, we observed improved stability of thin $CsPbI_3$ NC films without further additives or encapsulation procedures. Our work highlights the critical role of the solvent in the synthesis procedure in impacting the NCs' properties and stability.

Received 25th October 2025,
Accepted 14th April 2026

DOI: 10.1039/d5nr04491j

rsc.li/nanoscale

Open Access Article. Published on 12 May 2026. Downloaded on 6/30/2026 10:41:14 AM.
This article is licensed under a Creative Commons Attribution 3.0 Unported Licence.

Introduction

Colloidal nanocrystals (NCs) based on metal halide perovskites are a promising candidate for next-generation photovoltaics due to their unique optoelectronic properties, including size-tunable bandgap, high absorption coefficient, multiple exciton generation, and high defect tolerance.[1–4] Strategies such as surface modification,[5] and device architecture engineering,[6] quickly advanced the power conversion efficiency for solar cells of all-inorganic $CsPbI_3$ NCs from 10.77%[7] since its first publication to 17.5% in recent years.[8]

Among the various perovskite compositions, the all-inorganic cesium lead triiodide ($CsPbI_3$) is widely investigated due to its direct bandgap of ~1.7 eV, making it of great interest for application in tandem solar cells.[9] The main challenge preventing $CsPbI_3$ NCs' widespread application remains their poor stability – the NCs are prone to degrade to the non-photoactive phase (δ-$CsPbI_3$), considered the most thermodynamically stable at room temperature, whereas the photoactive, cubic α-phase in bulk $CsPbI_3$ is only stable at temperatures above 350 °C.[10,11] The tendency to convert to δ-$CsPbI_3$ is related to the relatively small ionic radius of Cs and the low Goldschmidt tolerance factor, which results in a slight distortion in the crystal structure.[12] Several strategies have been developed to improve the stability of $CsPbI_3$ NCs. Synthetic approaches focused primarily on the introduction of divalent cations. For example, Ji *et al.* reported that introducing Mn^{2+},[13] into the nanocrystals significantly enhanced their phase stability, with a similar strategy later applied by Wang *et al.* with Ni^{2+}.[14] Alternatively, enhancements in phase stability were achieved by surface passivation of the NCs.[15] For example, Li *et al.* reported using a poly-vinylpyrrolidone (PVP) polymer to stabilize α-$CsPbI_3$ NCs. More recently, Liu *et al.* reported a strategy to stabilize $CsPbI_3$ NCs by capping them with organic ligands, which consist of a polystyrene segment with hydroxyl and azide end groups.[16] However, one important aspect of NCs synthesis, *i.e.*, the solvent used, has not been explored as a means to improve the stability of the NCs, despite the fact that in other types of NCs it is known to have a significant impact on preferential orientation and crystallization.[17]

Indeed, since their first report by Protesescu and collaborators a decade ago, inorganic perovskite nanocrystals have been commonly synthesized using octadecene (ODE).[1,3–8]

[a]*Chair for Emerging Electronic Technologies TUD Dresden University of Technology, Nöthnitzer Straße 61, 01187 Dresden, Germany. E-mail: y.vaynzof@ifw-dresden.de*
[b]*Leibniz Institute for Solid State and Materials Research Dresden, Helmholtzstraße 20, 01069 Dresden, Germany*

Open Access Article. Published on 12 May 2026. Downloaded on 6/30/2026 10:41:14 AM.
This article is licensed under a Creative Commons Attribution 3.0 Unported Licence.

While synthesis in ODE proved effective, ODE is known to start to polymerize into poly(ODE) upon heating above 120 °C, and these byproducts can be challenging to remove even with harsh solvents/anti-solvent strategies.[18] These impurities reduce the stability and processability of the NCs since the purification steps can lead to ill-formed nanocrystals. To overcome the formation of poly(ODE), saturated solvents have been proposed as more inert alternatives, yet no reports exist exploring their suitability for $CsPbI_3$ NC synthesis.

This study investigates the efficacy of octadecane (ODA), a saturated hydrocarbon with properties similar to ODE, for synthesizing $CsPbI_3$ NCs. ODA is less reactive under high temperatures and is sometimes described as an inert solvent.

We synthesized and characterized the colloidal solutions' morphological, optical, and chemical properties. We demonstrate that replacing ODE with ODA impacts the phase distribution of the NCs, narrows their size distribution, and enhances their stability. Our study contributes to a better understanding of the role of the solvent choice during the NC synthesis and offers a simple approach to improving the all-inorganic perovskite NCs' stability without additional processing steps.

Results and discussion

Synthesis procedure

The synthesis of the $CsPbI_3$ NCs (Fig. 1) followed the hot-injection method developed by Protesescu,[1] with several modifications described in the Experimental section and our previous study to improve the quality of the NCs.[19] Here, we explore two different solvents, ODE and ODA, on their own and as mixtures to evaluate their impact on the properties and stability of the NCs. The relative amounts of ODE and ODA present during the synthesis are shown using the notation $ODE_{X-100}ODA_X$, with X = 0%, 25%, 50%, 75%, and 100%. After synthesis, the NCs were purified and kept as a colloid dispersion in octane to conduct structural, morphological, and optical characterization, as well as further analysis. All the analyses were performed with the purified NCs, unless stated otherwise.

Morphologic analysis and size distribution

We recorded transmission electron microscopy (TEM) images and analyzed them to explore how the solvent affects the crystalline phase, structure, and shape of the $CsPbI_3$ NCs. As shown in Fig. 2, we observe a progressive reduction in the polydispersion index (σ) from Fig. 2a 0.31 to Fig. 2e 0.16 while reducing the amount of ODE in the synthesis solution, whereas the overall average size of the NC remains similar. It is essential to mention that the morphological analysis was performed with purified NCs, for which the subsequent use of solvent/anti-solvent is known to damage the NCs' surface in each step of the washing procedure. Some studies have shown that the polydispersion of $CsPbI_3$ NCs increases with further purification.[20] Our study, however, shows that by only changing the solvent during the synthesis, we can reduce the polydispersity while still removing the excess of ligands; and the effect persists throughout the washing. In addition, the TEM images reveal better-defined and sharper NC edges (see especially Fig. 2e) in the case of ODA, in stark contrast to the high polydispersity and ill-defined morphology of the NCs synthesized using plain ODE. A possible reason for this obser-

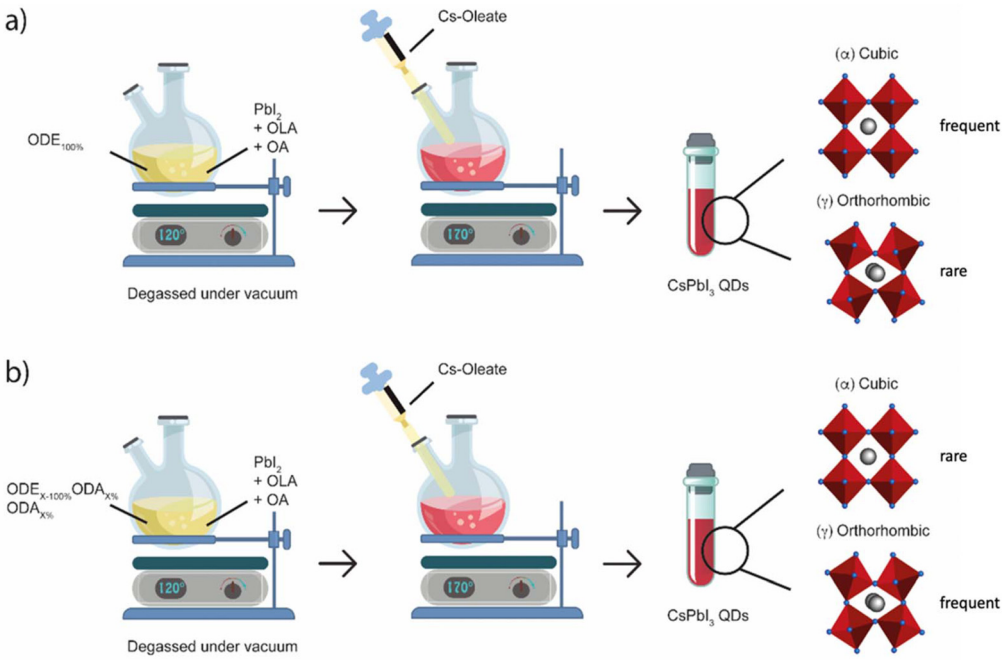

Fig. 1 Scheme of the hot injection protocol with (a) $ODE_{100\%}$, and (b) $ODA_{X\%}$ (where X refers to the percentage of ODA present in the synthesis); followed by the crystal structure present in the final solution.

This journal is © The Royal Society of Chemistry 2026

Open Access Article. Published on 12 May 2026. Downloaded on 6/30/2026 10:41:14 AM.
This article is licensed under a Creative Commons Attribution 3.0 Unported Licence.

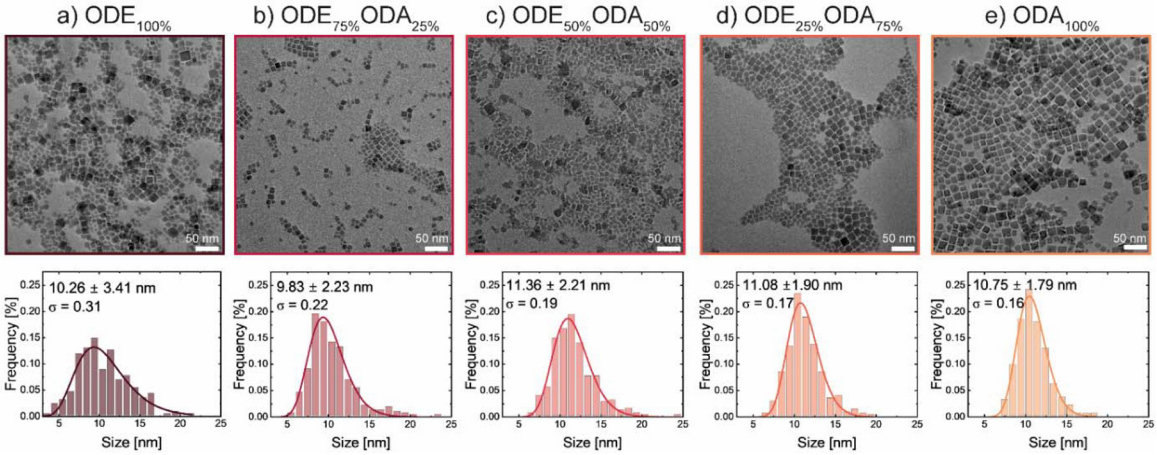

Fig. 2 TEM images and respective histograms with mean size and polydispersity index (σ) from samples of $CsPbI_3$ NCs by using different ratios of ODE/ODA (a) $ODE_{100\%}$, (b) $ODE_{75\%}ODA_{25\%}$, (c) $ODE_{50\%}ODA_{50\%}$, (d) $ODE_{25\%}ODA_{75\%}$, and (e) $ODA_{100\%}$.

vation is the difference in stability between NCs synthesized with ODE and ODA as solvents. This likely results in higher degradation of perovskite NCs synthesized in ODE during post-synthetic purification and TEM sample preparation.[18] Another consideration is that ODA is less reactive due to its saturated organic chain; thus, less damage to the NCs' surfaces could be expected.[11,12] In addition, the shape of the NCs seems to be affected, and more rectangular-shaped NCs seem to be present for increasing amounts of ODA. This will be analyzed and discussed in more detail in the following.

Optical properties, composition, and crystalline structure

The steady-state ultraviolet-visible (UV-vis) absorption and photoluminescence (PL) spectra, shown in Fig. 3a, exhibit little dependence on the solvent used in synthesis. As previously observed in the TEM images, the nanocrystal sizes are similar for all NCs. Consequently, only minor changes in the absorption spectra are expected. We determined the band gap of the NCs *via* a Tauc plot (Fig. S1), resulting in values around 1.79–1.81 eV. The PL measurements, therefore, show similar emission peaks for all NCs with an emission centered around ~690 nm with only a minor shift between the samples.[21] To evaluate the composition of the $CsPbI_3$ NCs, we conducted X-ray photoemission spectroscopy (XPS) measurements. Table S1 shows that all NCs exhibit the expected elemental ratios between Cs/Pb/I, independent of the solvent used during synthesis. The elements' binding energies were not impacted by the choice of solvent either (Fig. S2), confirming compositionally similar NCs. We can observe symmetric core peaks where the binding energies at 138.56 eV from Pb $4f_{7/2}$ can be well assigned to Pb(II), the 724.98 eV from Cs $3d_{5/2}$ to Cs(I), and the peak at 619.44 eV from $I_{3d5/2}$ to I(−I).[22–24] None of the samples exhibited metallic Pb, the absence of which has been shown to be beneficial for efficient radiative recombination.[25]

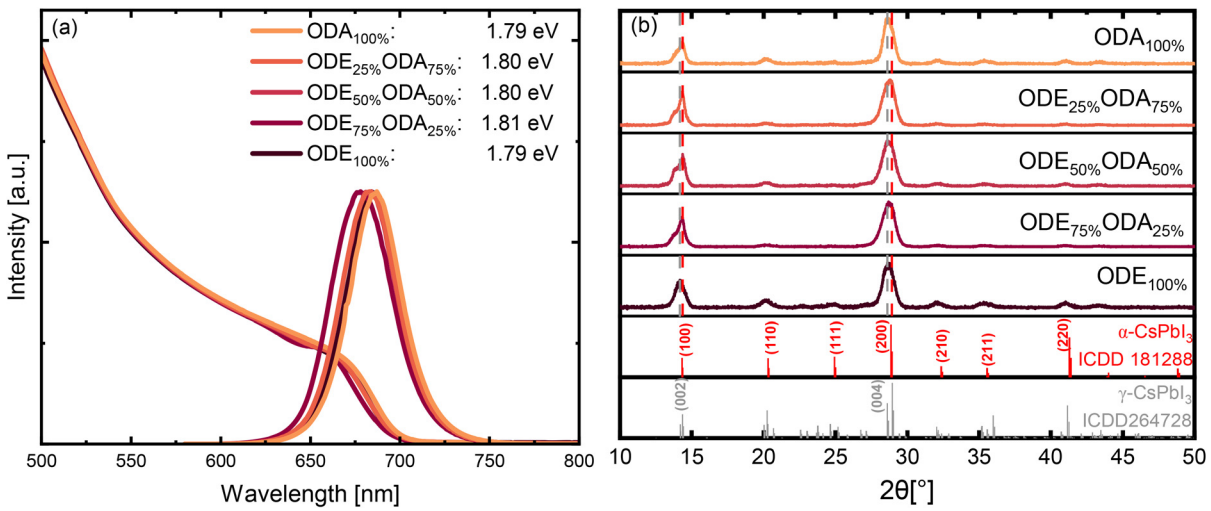

Fig. 3 Normalized measurements of (a) steady-state PL and UV-Vis; (b) XRD with respective patterns of ICDD264725 (γ-$CsPbI_3$) and ICDD181288 (α-$CsPbI_3$) – vertical dashed lines are aligned with diffraction peaks.

Open Access Article. Published on 12 May 2026. Downloaded on 6/30/2026 10:41:14 AM.
This article is licensed under a Creative Commons Attribution 3.0 Unported Licence.

The diffractograms in Fig. 3b show systematic reflections attributed to $CsPbI_3$ perovskite NCs. In the case of plain ODE, the broad reflections agree with the cubic α-phase, with the main preferential orientation corresponding to the (h00) planes. Interestingly, the diffractograms of NCs synthesized in ODE/ODA mixtures show additional reflection occurring at approximately 14°, and a slight shift of the central peak at 28°, which can be better observed in the zoomed-in graph in Fig. S3. The reflection at 14° appears to separate into multiple reflections, while the main peak at the higher angle matches the (002)-reflection from the orthorhombic γ-$CsPbI_3$ phase according to the ICDD 264728.[25,26] Alternatively, the peak splitting could also be attributed to the formation of superstructures, sometimes also called superlattice reflections. This effect combines two characteristics: high crystallinity, well-defined and identical shapes, and the regular packing with slight variation in the NCs spacing.[27]

To distinguish between the two possibilities and explore the potential formation of the γ-$CsPbI_3$ phase, we conducted high-resolution TEM (HR-TEM) experiments for the particles synthesized with either 100% ODA or 100% ODE (Fig. 4). The discrimination of the orthorhombic and cubic phase of the $CsPbI_3$ nanoparticles was based on the structure models given by Marronnier:[28] The crystal structure of the cubic phase has a $Pm\bar{3}m$ space group symmetry, and a lattice constant of a_c = 6.2966 Å (measured at 640 K). The structure of the orthorhombic has a $Pbnm$ space group symmetry and lattice constants a_o = 8.1697 Å, b_o = 8.8518 Å, c_o = 12.5013 Å (measured at 300 K). The orthorhombic lattice shows distorted pseudo-cubic units with a lattice constant of $c_o/2$ in c-axis direction and one-half of the diagonals in the a–b plane, which makes the discrimination between the two lattices based on lattice parameters complicated. This pseudo-cubic symmetry is observable in $[001]_o$ and in $[1{-}10]_o$ zone axes. The orthorhombic phase, however, exhibits additional characteristic reflections being absent in the cubic phase due to the larger unit cell. In $[001]_o$ and $[1{-}10]_o$, the characteristic reflections are indexed by [hk0] with $h + k$ = odd and [hkl] with l = odd, respectively (Fig. 4a and c). The cubic phase can be identified by the absence of these reflections in the $[100]_c$ zone axis

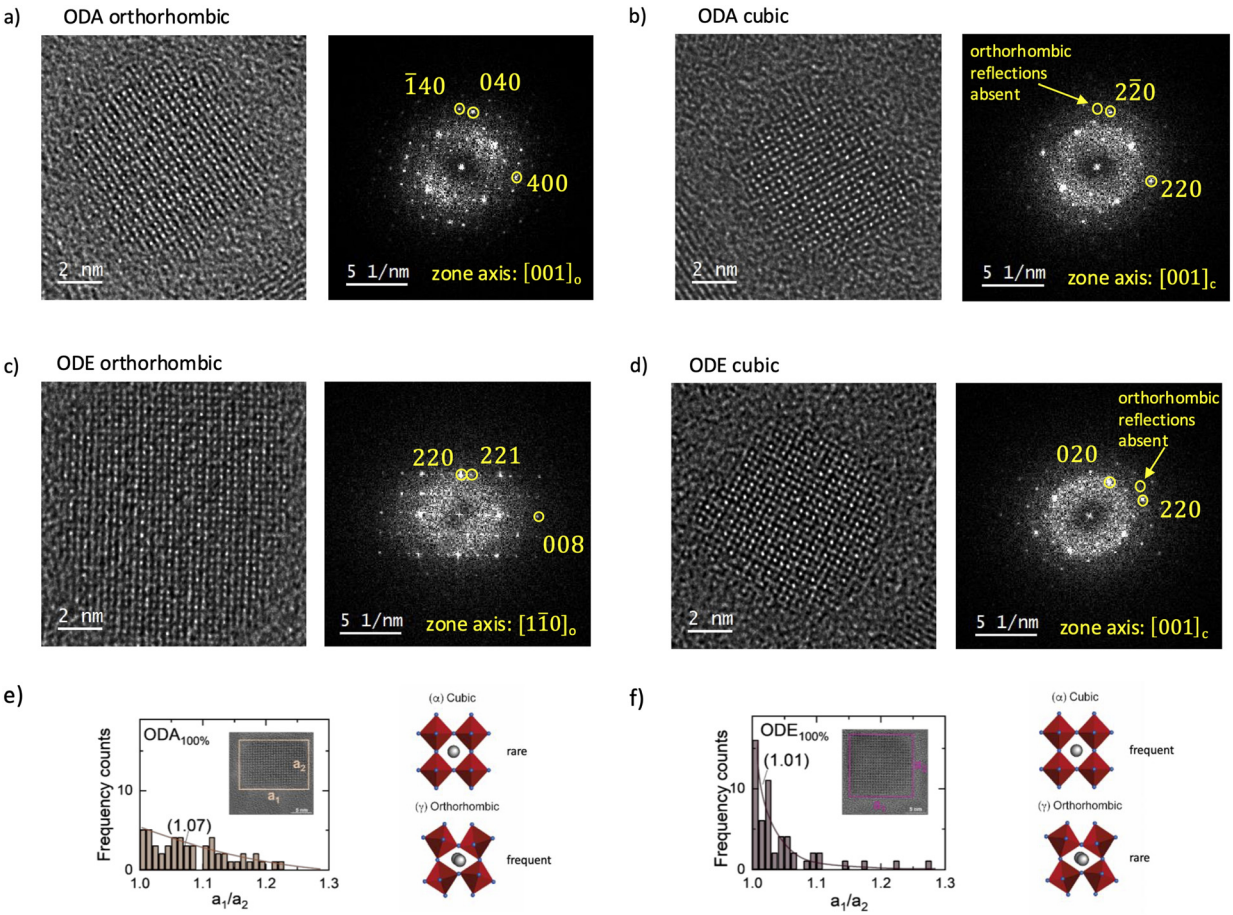

Fig. 4 HR-TEM images of ODA (a, b) and ODE (c, d) nanoparticles. (a) and (c) indicate particles of orthorhombic phase in $[001]_o$ and $[1{-}10]_o$ orientation, respectively, identified by the presence of the corresponding characteristic reflections. The particles in (b) and (d) exhibits cubic phase instead because of the absence of characteristic reflections and a better fit to the cubic structure model. The χ^2 values per degree of freedom (dof) are summarized in Table 1. The experimental measurements of the reciprocal lattice vectors and the best fitting zone axis parameters are compiled in the SI and Table S2. Frequency analysis of particle aspect ratio for (e) ODA and (f) ODE images from Fig. 2.

This journal is © The Royal Society of Chemistry 2026

Open Access Article. Published on 12 May 2026. Downloaded on 6/30/2026 10:41:14 AM.
This article is licensed under a Creative Commons Attribution 3.0 Unported Licence.

Table 1 χ^2 per degree of freedom for the comparison of the experimental data of Fig. 4b (ODA cubic) and Fig. 4d (ODE cubic) with the orthorhombic and cubic crystal structure

	ODA cubic	ODE cubic
$\frac{\chi^2}{\mathrm{dof}}$ orthorhombic $[1\bar{1}0]^{\mathrm{o}}$	0.0388	0.0385
$\frac{\chi^2}{\mathrm{dof}}$ cubic $[110]_{\mathrm{c}}$	**0.0201**	**0.0303**

(Fig. 4b and d). Note that a correction of the thermal expansion by assuming a typical coefficient of $\alpha = 20 \times 10^{-6}$ K^{-1} will not affect the discrimination presented here.

While HR-TEM is a powerful tool for atomic-resolution identification of crystal phases of NCs, the analysis remains very local, lacking statistical significance with respect to the relative prevalence of both types of structures in the ODA and ODE system. To further investigate the differences between the ODA and ODE nanocrystals, we therefore re-analyzed the TEM images shown in Fig. 2a and e. Specifically, we focused on particle shape analysis by assessing the aspect ratio (a_1/a_2) to distinguish between cubic (a_1/a_2 = 1) and rectangular particles (a_1/a_2 > 1). Fig. 4e and f show that ODE synthesis results in more cubic-shaped particles, whereas ODA particles are primarily rectangular. The prevalence of rectangular nanocrystals likely indicates that they are γ-$CsPbI_3$, in agreement with the ODA diffractograms in Fig. 3b.[25,26] However, further investigations are required to explore the mechanisms behind this shape change in more detail.

Stability of $ODE_{100\%}$ *vs.* $ODA_{100\%}$ samples

To evaluate the stability of the NCs synthesized using the two solvents, we deposited the $CsPbI_3$ NCs on glass substrates by spin-coating. The thin films consisted of four NC layers, where, following the deposition of each layer, the NCs were treated with sodium acetate (NaOAc), followed by three washes with methyl acetate (MeOAc).[28] Fig. 5a shows that samples prepared with $ODE_{100\%}$ lost their absorption and degraded to the yellow phase after only 1 hour. This transformation is significantly slower in thin films prepared using $ODA_{100\%}$, as observed in Fig. 5b, in which we still can observe notable absorption even after 24 h. Only after 48 h of continuous illumination from a Deuterium lamp at 300 nm of the spectrometer, the $ODA_{100\%}$ films degrade. Storage stability (kept in the ventilated cabinet) in the dark revealed similar results, ODE films degraded to the yellow phase within the first hours, whereas ODA films remained in the photoactive perovskite phase for 24 h (see images as insets in Fig. 5a and b).

We also evaluated the stability of the nanocrystals in solution by measuring their photoluminescence (PL), PL lifetimes, and photoluminescence quantum yield (PLQY) (Fig. 5c–e). For these experiments, we diluted the samples in octane and exposed them to ambient conditions for nine days. We observe that directly after synthesis (day 1), the PL intensity of the ODE sample is higher than that of ODA, but on subsequent days, ODA shows higher PL intensity. This trend can also be visualized by following the decline in the PLQY. The decrease in PL can be associated with the conversion of the nanocrystals to the δ-$CsPbI_3$ (non-photoactive phase), suggesting that this process is slowed down in ODA-synthesised nanocrystals. Interestingly, we consistently observe longer PL lifetimes (37.2–39.4 ns) in ODA-synthesised nanocrystals than in the ODE-synthesised samples (27–29.9 ns), suggesting reduced non-radiative recombination pathways.

To identify the origin of the differences in stability, the NCs were characterized using Fourier-transform infrared spectroscopy (FTIR) and nuclear magnetic resonance (NMR) spectroscopy to exclude differences in NC purity or ligand household between the ODA and ODE synthesis. We first performed FTIR measurements to gain insights into the composition of the NC dispersion after washing. The features shown in Fig. S4 originate primarily from C–H vibrations. The band between 2850 and 3000 cm^{-1} corresponds to the C–H stretch, the one at 1370 and 1470 cm^{-1} to in-plane C–H bending, and at 723 cm^{-1} to C–H out-of-plane bending.[29,30] The bands between 900 and 1350 cm^{-1} are quite low in intensity and hard to identify, but can be related to C–O, C–N, and N–H vibrations, in line with the presence of oleyl amine (OLA) and oleic acid (OA). A comparison between the FTIR results revealed no significant differences in ligand household for the ODA and ODE NCs.

To further investigate the ligands, we also performed NMR measurements, which are more sensitive to small changes in the synthesis. Fig. S5 also shows relatively minor differences between the samples, matching the FTIR results. In the case of NCs synthesized using ODE, NMR analysis shows the presence of ODE impurities even after purification, with peaks around 5.0 and 5.8 ppm corresponding to alkene groups of ODE.[18] Both samples contain a broad signal at 5.55 ppm of bound organic ligands on the surface of the NCs (OA and OLA). This type of surface passivation is already known in the literature, since long ligands have been used to stabilize the particles and increase the shelf storage and overall stability.[7,29] Since the NCs exhibited similar composition in terms of the organic ligands, these results suggest that the improved stability of the ODA NCs arises from the increased prevalence of the more stable orthorhombic phase of the $CsPbI_3$.

Identifying the exact mechanism by which the formation of γ-$CsPbI_3$ seems more likely when ODA is used is highly complex. ODA may impact the nucleation and/or growth of the NCs due to several factors. For example, the viscosity of ODA is different from that of ODE. The solubility of the ligands used during the synthesis (OA, OLA) also varies between ODE and ODA. Moreover, ODA may mediate the binding equilibrium of ligands, resulting in better passivation of a specific facet, thus enabling anisotropic growth. These and possibly other factors, on their own or in combination, may impact the formation of NCs with different phases, either γ-$CsPbI_3$ or α-$CsPbI_3$.[25,30–32]

Finally, to explore the use of other inert solvents, we also performed experiments with heptadecane, tetradecane, and liquid paraffin. We find that all three solvents are suitable for the syn-

Open Access Article. Published on 12 May 2026. Downloaded on 6/30/2026 10:41:14 AM.
This article is licensed under a Creative Commons Attribution 3.0 Unported Licence.

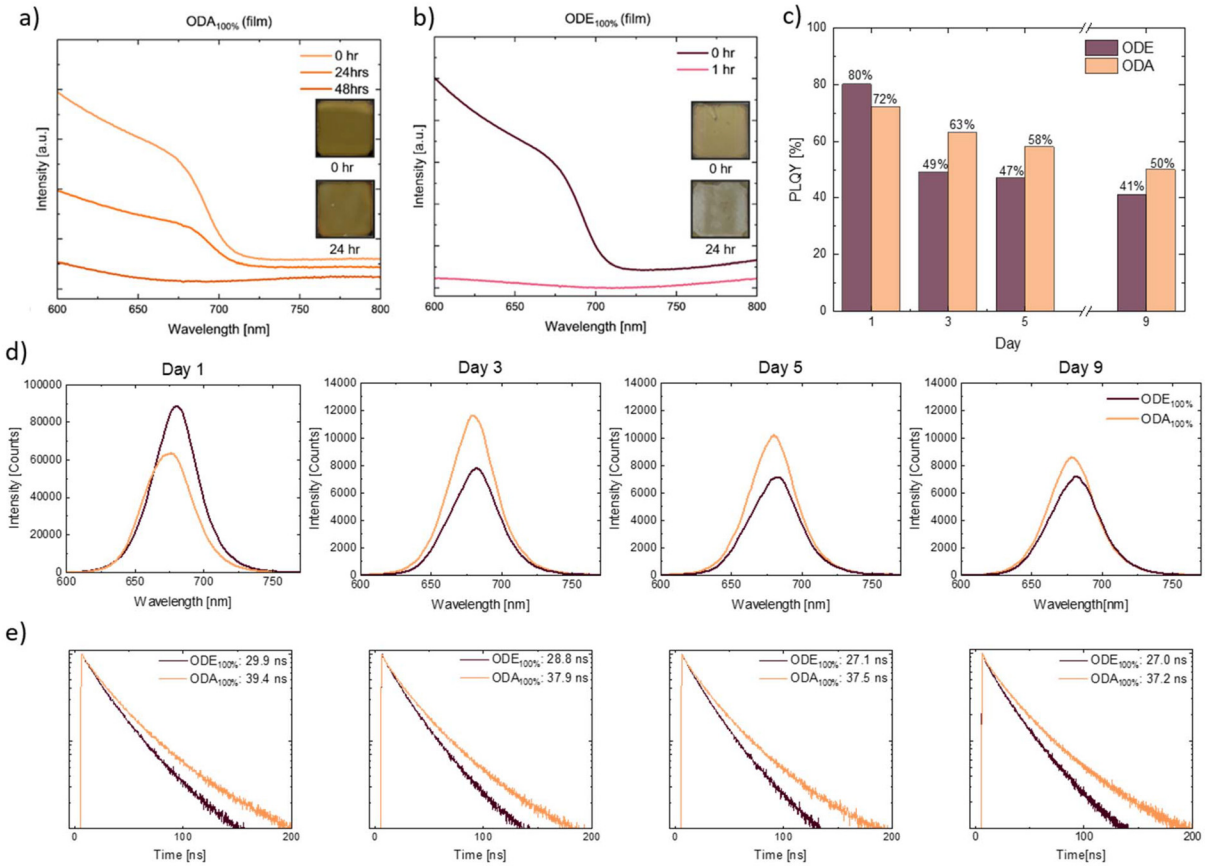

Fig. 5 Temporal evolution of Uv-vis spectra of thin $CsPbI_3$ NC films under continuous illumination (Deuterium lamp at 300 nm) from (a) $ODA_{100\%}$ and (b) $ODE_{100\%}$ with respective images of the films after storage for 24 h as insets; the (c) PLQY shows the trend of the liquid samples over 9 days, followed by the (d) PL intensity and (e) time-decay from the samples.

thesis of $CsPbI_3$ and lead to a narrower size distribution than ODE (Fig. S6). We also observe an increase in the mean nanocrystal size, especially for liquid paraffin. However, a closer analysis of the TEM images reveals that using heptadecane or tetradecane results in residual unreacted lead iodide (PbI_2) in the solution even after purification. This suggests that using these solvents would require re-optimization of the synthesis and purification protocols, which falls beyond the scope of the current study. The optical measurements (Fig. S7a) show a small shift in the band gap, likely due to differences in mean particle size across the samples, with larger nanocrystals having smaller band gaps than smaller ones. The XRD diffractograms (Fig. S7b) also show an additional contribution from the (002) reflection, but it is not as clearly evident as in the samples prepared with ODA and the respective ODA : ODE mixtures.

Conclusions

We report that ODA is a suitable solvent for synthesizing $CsPbI_3$ *via* a hot-injection procedure. A careful characterization of the NCs revealed that the choice of solvent impacts the size distribution and the prevalence of α- and γ-$CsPbI_3$ NCs. NCs synthesized using ODE, a ubiquitous solvent for perovskite NC synthesis, showed a large polydispersity index of 0.31 and predominantly cubic-shaped dots of α-$CsPbI_3$. ODA, on the other hand, leads to a starkly reduced polydispersity index of 0.16 and an increase in the prevalence of γ-$CsPbI_3$ NCs. Consequently, differences in the stability of solutions and thin films fabricated using both NC inks were observed, with ODA films and solutions being more stable than ODE. These results demonstrate that the solvent used for NC synthesis plays an important role and must be considered. Future studies may explore other saturated solvents as a promising strategy to stabilize $CsPbI_3$ NCs and other perovskite compositions.

Experimental section

Materials

All chemicals were used without further purification. Cs-carbonate (Cs_2CO_3 > 99.9%), oleic acid (OA; technical grade, 70%), oleylamine (OLA; technical grade, 70%), sodium acetate (NaOAc; 99.995%), octadecane (ODA, 99%), octadecene (ODE, 90%), heptadecane (99%), tetradecane (99%) and liquid paraffin (90%) were purchased from Sigma Aldrich. Lead iodide (PbI_2; 99.99%) was obtained from TCI. Methyl acetate

This journal is © The Royal Society of Chemistry 2026

Open Access Article. Published on 12 May 2026. Downloaded on 6/30/2026 10:41:14 AM.
This article is licensed under a Creative Commons Attribution 3.0 Unported Licence.

(MeOAc; 99%), hexane (97%), and octane (99%) were bought from Acros Organics.

Synthesis procedure

Cs(oleate). Cesium oleate precursor was prepared by loading 0.5 g of Cs_2CO_3 into a two-neck flask, along with OA (2 mL) and ODE (50 mL). The mixture was degassed in a vacuum at a Schlenk line for 1 hour at 100 °C under constant stirring. The flask was then kept under nitrogen flow at 150 °C until the Cs_2CO_3 powder was completely dissolved and a transparent solution was achieved. The solution was then stored in nitrogen at 70 °C until usage. For the different ratios, the ODE and ODA were adjusted accordingly with the desired percentage of the solvent ($ODE_{75\%}ODA_{25\%}$, $ODE_{50\%}ODA_{50\%}$, and $ODE_{25\%}ODA_{75\%}$).

$CsPbI_3$ nanocrystals. The synthesis of $CsPbI_3$ nanocrystals follows the hot injection procedure published by Protesescu *et al.*, with several modifications. PbI_2 (1.008 g) was placed into a three-neck flask with ODE (60 mL), followed by 1 hour of degassing at 120 °C under constant stirring. Then, OA (6 mL) and OLA (6 mL) were injected and left to degas for 30 minutes. The mixture was subsequently heated in a nitrogen atmosphere until reaching 170 °C. At this temperature, Cs(oleate) (8 mL) was rapidly injected into the flask while stirring. After 7 seconds, the reaction was quenched with an ice bath. The purification process followed the synthesis: the fresh $CsPbI_3$ NC solution was split into four centrifuge tubes, each containing the crude solution (20 mL) and MeOAc (20 mL), then centrifuged for 3 minutes at 10 621 rcf. The supernatant was discarded, and the precipitate was dissolved in hexane (3 mL) from each tube. This solution was then mixed with MeOAc (3.5 mL) and centrifuged for 3 minutes at 10 621 rcf. The supernatant was discarded again, and the precipitate from all tubes was dissolved in octane (2 mL). After centrifuging for 5 minutes at 4248 rfc, the precipitate was discarded, and the upper solution was collected and stored in the fridge at 4 °C overnight. Subsequently, the solution was centrifuged for 5 minutes at 4248 rfc, and the supernatant was collected. The concentration was determined optically and adjusted to 75 mg mL^{-1} for further use. The procedure was consistently followed for the different solvents using the target ratios between ODE and ODA ($ODE_{75\%}ODA_{25\%}$, $ODE_{50\%}ODA_{50\%}$, and $ODE_{25\%}ODA_{75\%}$). For samples produced with any volume of ODA, the solvent had to be pre-heated, since the solvent is solid at room temperature. The synthesis procedure using the heptadecane, tetradecane, and liquid paraffin followed the same approach, only replacing the used solvent.

Thin-films fabrication

For stability investigation, we prepared thin films as previously reported with slight modifications.[19] Glass substrates were cleaned by sonication with acetone and 2-propanol for 15 minutes each. The samples were then subjected to oxygen plasma for 10 minutes to remove organic residues. For the spin-coated deposition, the substrates and NC solution were transferred to a nitrogen-filled glovebox. The NC solution obtained from the synthesis, with a concentration of 75 mg mL^{-1}, was then spin-coated dynamically on the substrate at 1000 rpm for the first 5 s and 2000 rpm for the following 10 s. To remove excess long organic ligands, the film was immersed in a saturated NaOAc solution in MeOAc (1 mg mL^{-1}) for 15 s and spin-dried, then soaked and spin-dried in MeOAc for 5 s, three times. The procedure was repeated four times to obtain a compact film.

Optical, morphological, and chemical characterization

X-ray diffraction. Samples for XRD were prepared by drop-casting the solution on glass substrates. The measurements were performed in air. Diffractograms were obtained using a Bruker Avance D8 diffractometer equipped with a 1.6 kW Cu-Anode (λ = 0.154060 Å), and a 2 mm slit. All scans were performed using 1D mode with LYNXEYE_XE_T in parallel beam geometry. The scan was performed from 10° to 50°, with a step size of 0.01°, and an acquisition time of 0.1 s per step. The background was removed using the Bruker Diffrac.Eva software.

Optical absorbance. Absorbance measurements were conducted in air using a JASCO UV-vis spectrometer V-770. Cuvettes were sealed to minimize the environmental exposure. For long-term measurements, we prepared thin films, and during the measurements, the samples were kept under constant exposure to a Deuterium lamp at 300 nm from the JASCO UV-vis spectrometer V-770. No encapsulation was used for these measurements.

Photoluminescence (PL), Photoluminescence Quantum Yield (PLQY), and TRPL measurements: PL and PLQY measurements were performed on a FluoTime 3000 photoluminescence spectrometer, using the laser 509 nm excitation source with a repetition rate of 2 MHz. Octane was used as a solvent in order to dilute and prepare the samples for measurements. To track the stability of the nanoparticles in solution by PL and TRPL, the cuvettes were kept in air and under ambient light in a fume hood. The TRPL data were fitted using a biexponential function.

Transmission electron microscope (TEM). The transmission electron microscope (TEM) images were taken using a JEOL F200 microscope at 200 kV acceleration voltage. The diluted solution of NCs was drop-cast on a TEM copper grid. The images were analyzed using ImageJ software for particle shape and size distributions. The mean size and polydispersity index were obtained using the LogNormal function with Origin software. Further high-resolution TEM images were acquired at 300 keV using an aberration-corrected ThermoFisher Titan 80-300 TEM equipped with a Gatan OneView Camera Model 1095. The magnification calibration was confirmed by a gold reference sample. The description of the reciprocal lattice and best fitting parameters is summarized in the SI, page S4, together with the calculations in Table S2.

Nuclear magnetic resonance (NMR). Data were recorded at ambient temperature on a Bruker AV-II 300 spectrometer operating at 300 MHz.

X-ray photoemission spectroscopy (XPS). XPS measurements were carried out in an ultrahigh vacuum chamber (ESCALAB 250Xi by Thermo Scientific, base pressure: 2×10^{-10} mbar) using an XR6 monochromated Al Kα source ($h\nu$ = 1486.6 eV) and a pass energy of 20 eV. A spot size of 650 μm was utilized

Open Access Article. Published on 12 May 2026. Downloaded on 6/30/2026 10:41:14 AM. This article is licensed under a Creative Commons Attribution 3.0 Unported Licence.

for the analysis. Samples for XPS measurements were spin-coated on ITO substrates. All measurements were performed in the dark.

Fourier transform infrared spectroscopy (FTIR). Aliquots were removed after purification of the synthesis procedure and drop-cast in a KBr pellet to measure FTIR. 30 mg of KBr was ground in a mortar and later pressed into a pellet with a pressure of 1.7 t and a mini pellet press of 7 mm diameter (Specac). A pure KBr pellet was used for the background measurement. Lastly, the measurements were performed using an IRSprit from Shimadzu, averaging 20 measurements.

Author contributions

R. P. Muniz undertook the synthesis experiments and preliminary investigation, including experiments, analysis, and preparation of the original manuscript draft. J. Brunner helped with conducting TEM measurements and collaborated on the synthesis and discussion of the work. A. Prudnikau conducted HR-TEM acquisitions and analyzed the NMR data. R. D. Campos performed and analyzed the FTIR data. S. Singh performed and analyzed XPS measurements for the samples. F. Röder performed the analysis of the HR-TEM study by fitting structure models to diffraction data with the support of A. Lubk. Y. Vaynzof conceptualized the study and acquired funding. F. Paulus and Y. Vaynzof supervised the project. All the authors contributed to reviewing and editing the submitted version.

Conflicts of interest

There are no conflicts to declare.

Data availability

The datasets generated during and/or analysed during the current study are not publicly available due to potential protection, but are available from the authors on reasonable request.

Supplementary information (SI): Tauc-plots, XPS, XRD, NMR, FTIR, HR-TEM data and experimental details, TEM, UV-vis and PL. See DOI: https://doi.org/10.1039/d5nr04491j.

Acknowledgements

A. P. and F. P. thank the German Federal Ministry for Science, Technology, and Space (BMFTR) for funding through the project “GreenDots” (FK 03XP0422A). R. P. M. and Y. V. thank the DFG for generous support within the framework of the GRK 2767 (project A7). S. S. and Y. V. also acknowledge Marie Skłodowska–Curie grant agreement no 101066273. The authors thank Israel Noel for NMR measurements and the Dresden Center for Nanoanalysis (DCN) for access to the TEM microscope. The authors acknowledge financial support from the Leibniz-Kooperative Exzellenz project K524/2023.

References

1 L. Protesescu, S. Yakunin, M. I. Bodnarchuk, F. Krieg, R. Caputo, C. H. Hendon, *et al.*, Nanocrystals of Cesium Lead Halide Perovskites ($CsPbX_3$, X = Cl, Br, and I): Novel Optoelectronic Materials Showing Bright Emission with Wide Color Gamut, *Nano Lett.*, 2015, **15**(6), 6, DOI: 10.1021/nl5048779.

2 M. Li, R. Begum, J. Fu, Q. Xu, T. M. Koh, S. A. Veldhuis, *et al.*, Low threshold and efficient multiple exciton generation in halide perovskite nanocrystals, *Nat. Commun.*, 2018, **9**(1), 4197, DOI: 10.1038/s41467-018-06596-1.

3 Y. Li, M. Deng, X. Zhang, T. Xu, X. Wang, Z. Yao, Q. Wang, L. Qian and C. Xiang, Stable and efficient $CsPbI_3$ quantum-dot light-emitting diodes with strong quantum confinement, *Nat. Commun.*, 2024, **15**, 5696, DOI: 10.1038/s41467-024-50022-8.

4 J. Song, J. Li, X. Li, L. Xu, Y. Dong and H. Zeng, Quantum Dot Light-Emitting Diodes Based on Inorganic Perovskite Cesium Lead Halides ($CsPbX_3$), *Adv. Mater.*, 2015, **27**(44), 7162–7167, DOI: 10.1002/adma.201502567.

5 X. Mei, G. Wang, J. Qiu, Z. Qi, M. Zhang, M. Yu, J. Liu and X. Zhang, Surface Stress Engineering of $CsPbI_3$ Perovskite Quantum Dots for Efficient Solar Cells, *Small*, 2025, **21**(22), 2500007, DOI: 10.1002/smll.202500007.

6 L. Hu, Q. Zhao, S. Huang, J. Zheng, X. Guan, R. Patterson, J. Kim, L. Shi, C.-H. Lin, Q. Lei, D. Chu, W. Tao, S. Cheong, R. D. Tilley, A. W. Y. Ho-Bailley, J. M. Luther, J. Yuan and T. Wu, Flexible and efficient perovskite quantum dot solar cells via hybrid interfacial architecture, *Nat. Commun.*, 2021, **12**(1), 466, DOI: 10.1038/s41467-020-20749-1.

7 A. Swarnkar, A. R. Marshall, E. M. Sanehira, B. D. Chernomordik, D. T. Moore, J. A. Christians, T. Chakrabarti and J. M. Luther, Quantum dot-induced phase stabilization of α-$CsPbI_3$ perovskite for high-efficiency photovoltaics, *Science*, 2016, **354**(6308), 92–95, DOI: 10.1126/science.aag2700.

8 H. Li, H. Huang, D. Li, X. Zhang, C. Zhao, X. Zhao, W. Ma and J. Yuan, Buried interface engineering enables efficient and refurbished $CsPbI_3$ perovskite quantum dot solar cells, *Energy Environ. Sci.*, 2025, **18**(2), 972–981, DOI: 10.1039/D4EE04628E.

9 J. Khan, I. Ullah and J. Yuan, $CsPbI_3$ perovskite quantum dot solar cells: opportunities, progress and challenges, *Mater. Adv.*, 2022, **3**(4), 1931–1952, DOI: 10.1039/D1MA01075A.

10 G. E. Eperon, G. M. Paternò, R. J. Sutton, A. Zampetti, A. A. Haghighirad, F. Cacialli and H. J. Snaith, Inorganic caesium lead iodide perovskite solar cells, *J. Mater. Chem. A*, 2015, **3**(39), 19688–19695, DOI: 10.1039/C5TA06398A.

11 C. C. Lin, S. K. Huang, C. E. Hsu, Y. C. Huang, C. Y. Wei, C. Y. Wen, S.-S. Li, C.-W. Chen and C.-C. Chen, Exploring the Origin of Phase-Transformation Kinetics of $CsPbI_3$ Perovskite Nanocrystals Based on Activation Energy Measurements, *J. Phys. Chem. Lett.*, 2020, **11**(9), 3287–3293, DOI: 10.1021/acs.jpclett.0c00443.

 This journal is © The Royal Society of Chemistry 2026

Open Access Article. Published on 12 May 2026. Downloaded on 6/30/2026 10:41:14 AM. This article is licensed under a Creative Commons Attribution 3.0 Unported Licence.

12 H. Näsström, P. Becker, A. J. Márquez, O. Shargaieva, R. Mainz, E. Unger and T. Unold, Dependence of phase transitions on halide ratio in inorganic $CsPb(Br_xI_{1-x})_3$ perovskite thin films obtained from high-throughput experimentation, *J. Mater. Chem. A*, 2020, **8**(43), 22626–22631, DOI: 10.1039/D0TA08067E.

13 Y. Ji, J. B. Zhang, H. R. Shen, Z. Su, H. Cui, T. Lan, J.-Q. Wang, Y.-H. Chen, L. Liu, K. Cao, W. Shen and S. Chen, Improving the Stability of α-$CsPbI_3$ Nanocrystals in Extreme Conditions Facilitated by Mn^{2+} Doping, *ACS Omega*, 2021, **6**(21), 13831–13838, DOI: 10.1021/acsomega.1c01383.

14 J. Wang, C. Zhang, S. Li, Q. Guo, Y. Bai and G. Jia, Simultaneous Enhancement of the Luminescence Intensity and Stability of Deep-Red $CsPbI_3$ Perovskite Quantum Dots Achieved by a Doping Strategy, *Langmuir*, 2023, **39**(32), 11317–11328, DOI: 10.1021/acs.langmuir.3c01007.

15 B. Li, Y. Zhang, L. Fu, T. Yu, S. Zhou, L. Zhang and L. Yin, Surface passivation engineering strategy to fully-inorganic cubic $CsPbI_3$ perovskites for high-performance solar cells, *Nat. Commun.*, 2018, **9**, 1076, DOI: 10.1038/s41467-018-03169-0.

16 X. Liu, J. Lv, S. Yao, Y. Wang, L. Peng, J. Chen, X. Liu, J. Lin and X. Chen, Surface-Stabilized $CsPbI_3$ Nanocrystals with Tailored Organic Polymer Ligand Binding, *Chem. – Eur. J.*, 2023, **29**(26), e202203971, DOI: 10.1002/chem.202203971.

17 N. A. Neisius, L. T. MacHale, E. R. Snyder, R. G. Finke and A. L. Prieto, Copper Selenophosphate, Cu3PSe4, Nanoparticle Synthesis: Octadecane Is the Key to a Simplified, Atom-Economical Reaction, *Nano Lett.*, 2023, **23**(24), 11430–11437, DOI: 10.1021/acs.nanolett.3c02620.

18 E. Dhaene, J. Billet, E. Bennett, I. Van Driessche and J. De Roo, The Trouble with ODE: Polymerization during Nanocrystal Synthesis, *Nano Lett.*, 2019, **19**(10), 7411–7417, DOI: 10.1021/acs.nanolett.9b03088.

19 J. Brunner, A. Wrzesińska-Lashkova, L. Scalon, R. P. Muniz, A. Prudnikau, D. Pohl, M. Löffler, F. Paulus and Y. Vaynzof, Post-Degradation Recovery of $CsPbI_3$ Quantum Dot Solar Cells, *Small*, 2025, **21**, 2409709, DOI: 10.1002/smll.202409709.

20 S. Lim, G. Lee, S. Han, J. Kim, S. Yun, J. Lim, Y.-J. Pu, M. J. Ko, T. Park, J. Choi and Y. Kim, Monodisperse Perovskite Colloidal Quantum Dots Enable High-Efficiency Photovoltaics, *ACS Energy Lett.*, 2021, **6**(6), 2229–2237, DOI: 10.1021/acsenergylett.1c00462.

21 F. Bertolotti, N. Dengo, A. Cervellino, M. I. Bodnarchuk, C. Bernasconi, I. Cherniukh, Y. Berezovska, S. C. Boehme, M. V. Kovalenko, N. Masciocch and A. Guagliardi, Size- and Temperature-Dependent Lattice Anisotropy and Structural Distortion in $CsPbBr_3$ Quantum Dots by Reciprocal Space X-ray Total Scattering Analysis, *Small Struct.*, 2024, **5**(3), 2300264, DOI: 10.1002/sstr.202300264.

22 Y. Hassan, Y. Song, R. D. Pensack, A. I. Abdelrahman, Y. Kobayashi, M. A. Winnik and G. D. Scholes, Structure-Tuned Lead Halide Perovskite Nanocrystals, *Adv. Mater.*, 2016, **28**(3), 566–573, DOI: 10.1002/adma.201503461.

23 F. Liu, Y. Zhang, C. Ding, S. Kobayashi, T. Izuishi, N. Nakazawa, T. Toyoda, T. Ohta, S. Hayase, T. Minemoto, K. Yoshino, S. Dai and Q. Shen, Highly Luminescent Phase-Stable $CsPbI_3$ Perovskite Quantum Dots Achieving Near 100% Absolute Photoluminescence Quantum Yield, *ACS Nano*, 2017, **11**(10), 10373–10383, DOI: 10.1021/acsnano.7b05442.

24 R. Lindblad, D. Bi, P. B. Wook, J. Oscarsson, M. Gorgoi, H. Siegbahn, M. Odelius, E. M. J. Johansson and H. Rensmo, Electronic Structure of $TiO_2/CH_3NH_3PbI_3$ Perovskite Solar Cell Interfaces, *J. Phys. Chem. Lett.*, 2014, **5**(4), 648–653, DOI: 10.1021/jz402749f.

25 J. Guo, M. Lu, X. Zhang, S. Sun, C. Han, Y. Zhang, X. Yang, S. V. Kershaw, W. Zheng and A. L. Rogach, Highly Stable and Efficient Light-Emitting Diodes Based on Orthorhombic γ-$CsPbI_3$ Nanocrystals, *ACS Nano*, 2023, **17**(10), 9290–9301, DOI: 10.1021/acsnano.3c00789.

26 R. J. Sutton, M. R. Filip, A. A. Haghighirad, N. Sakai, B. Wenger, F. Giustino and H. J. Snaith, Cubic or Orthorhombic? Revealing the Crystal Structure of Metastable Black-Phase $CsPbI_3$ by Theory and Experiment, *ACS Energy Lett.*, 2018, **3**(8), 1787–1794, DOI: 10.1021/acsenergylett.8b00672.

27 S. Toso, D. Baranov, C. Giannini, S. Marras and L. Manna, Wide-Angle X-ray Diffraction Evidence of Structural Coherence in $CsPbBr_3$ Nanocrystal Superlattices, *ACS Mater. Lett.*, 2019, **1**(2), 272–276, DOI: 10.1021/acsmaterialslett.9b00217.

28 A. Marronnier, G. Roma, S. Boyer-Richard, L. Pedesseau, J. M. Jancu, Y. Bonnassieux, C. Katan, C. C. Stoumpos, M. G. Kanatzidis and J. Even, Anharmonicity and Disorder in the Black Phases of Cesium Lead Iodide Used for Stable Inorganic Perovskite Solar Cells, *ACS Nano*, 2018, **12**(4), 3477–3486, DOI: 10.1021/acsnano.8b00267.

29 Y. Wang, J. Yuan, X. Zhang, X. Ling, B. W. Larson, Q. Zhao, Y. Yang, Y. Shi, J. M. Luther and W. Ma, Surface Ligand Management Aided by a Secondary Amine Enables Increased Synthesis Yield of $CsPbI_3$ Perovskite Quantum Dots and High Photovoltaic Performance, *Adv. Mater.*, 2020, **32**(32), 2000449, DOI: 10.1002/adma.202000449.

30 N. C. Anderson, M. P. Hendricks, J. J. Choi and J. S. Owen, Ligand Exchange and the Stoichiometry of Metal Chalcogenide Nanocrystals: Spectroscopic Observation of Facile Metal-Carboxylate Displacement and Binding, *J. Am. Chem. Soc.*, 2013, **135**(49), 18536–18548, DOI: 10.1021/ja4086758.

31 J. A. Steele, H. Jin, I. Dovgaliuk, R. F. Berger, T. Braeckevelt, H. Yuan, *et al.*, Thermal unequilibrium of strained black $CsPbI_3$ thin films, *Science*, 2019, **365**(6454), 679–684, DOI: 10.1126/science.aax3878.

32 H. Zhao, Y. Wang, C. Wang, A. K. Bandela and U. Thumu, Dissolution-Dictated Recrystallization in Cesium Lead Halide Perovskites and Size Engineering in δ-$CsPbI_3$ Nanostructures, *Cryst. Growth Des.*, 2023, **23**(10), 7412–7423, DOI: 10.1021/acs.cgd.3c00817.